

## Degradation of an internal wave beam by parametric subharmonic instability in an upper ocean pycnocline

B. Gayen<sup>1</sup> and S. Sarkar<sup>1</sup>

Received 25 March 2013; revised 16 July 2013; accepted 16 July 2013; published 20 September 2013.

[1] Numerical simulations are performed to investigate the interaction of a semidiurnal internal wave (IW) beam with the nonuniform stratification of an upper ocean pycnocline. During the initial stage of the interaction, higher harmonics originate after reflection of the IW beam at the caustic and are trapped in the pycnocline. In cases where the pycnocline thickness is sufficiently large (approximately larger than twice the dominant wavelength in the beam), the incoming beam undergoes a parametric subharmonic instability (PSI) during refraction through the pycnocline at later time. Consequently, there is significant energy transfer to subharmonic motions that exhibit exponential growth with a rate of  $2/3 \text{ day}^{-1}$ . The instability is demonstrated to be a resonant triad interaction by diagnostics in both wave frequency and wave number spaces. Smaller vertical scales originate during the PSI, lead to wave steepening, and produce convective overturns. This work identifies a potential mechanism that drives IW beam degradation during its propagation through the upper ocean.

**Citation:** Gayen, B., and S. Sarkar (2013), Degradation of an internal wave beam by parametric subharmonic instability in an upper ocean pycnocline, *J. Geophys. Res. Oceans*, 118, 4689–4698, doi:10.1002/jgrc.20321

### 1. Introduction

[2] Internal waves (IWs) generated by surface tidal flow over critical and supercritical topography form a tidal beam composed of many spatial modes within a finite-width region. After generation, an IW beam may traverse into the upper part of the ocean. During its propagation through a nonuniform stratified environment in the upper ocean, a beam encounters a region of density change (pycnocline) and there are observational studies [Martin *et al.*, 2006; Cole *et al.*, 2009; Holbrook *et al.*, 2009; Johnston *et al.*, 2010] that show degradation of the internal wave beam during its interaction with the pycnocline. The objective of the present work is to understand mechanisms leading to beam degradation in a pycnocline through a numerical process study.

[3] The cascade from internal tides to small spatial scales and eventual turbulence plays a significant role in deep-ocean mixing [Garrett, 2003] so as to maintain the vertical stratification observed in the mid-ocean. Mixing in the deep ocean conveys heat from the upper layer of the ocean to the abyssal cold waters balancing the upwelling of cold water and, thus, it helps to maintain the meridional overturning circulation. Apart from internal wave breaking near topography [Polzin *et al.*, 1997; Nash *et al.*, 2007;

Gayen and Sarkar, 2011a] or in critical layers, there can be nonlinear interaction between groups of propagating internal waves [Müller *et al.*, 1986] to generate further spatial scales and temporal frequencies. In particular, the formation of subharmonics with a higher vertical wave number than the original internal wave could constitute the first step in the breakdown of internal tides to turbulence. A single internal wave of frequency  $\omega_0$  and wave vector  $\mathbf{K}_0$  is subject to an instability under certain circumstances whereby the primary wave decays by transferring energy into two waves of lower frequency, such that  $\mathbf{K}_0 = \mathbf{K}_1 + \mathbf{K}_2$  and  $\omega_0 = \omega_1 + \omega_2$  are satisfied. This process is known as parametric subharmonic instability. The special case  $\omega_1 = \omega_2 \simeq \omega_0/2$  corresponds to maximum energy transfer in the limit of high wave numbers,  $k_1$  and  $k_2$ , of the subharmonics [Staquet and Sommeria, 2002]. PSI with energy partitioning into unequal frequencies is also possible. For instance, Korobov and Lamb [2008] found PSI involving  $\omega_0$ ,  $0.57\omega_0$ , and  $0.43\omega_0$  in numerical simulations of internal tide generation at a flat-topped ridge. Recently, Bourget *et al.* [2013] identified PSI involving  $\omega_0$ ,  $0.67\omega_0$ , and  $0.33\omega_0$  in their laboratory experiments and theoretically showed that the selection of participating frequencies and instability growth rate depends on the frequency, wave number, and Reynolds number of the primary wave.

[4] Internal wave beams have been observed near generation [Pingree and New, 1989] and after bottom reflection [Pingree and New, 1991] in the Bay of Biscay. Semidiurnal IW beams, originating from Kaena Ridge in Kauai Channel, have been observed and their structure studied by Martin *et al.* [2006], Cole *et al.* [2009], and Pickering and Alford [2012]. There is evidence of interaction with the upper ocean pycnocline that degrades the beams generated at Kaena Ridge during their interaction with the upper

<sup>1</sup>Mechanical and Aerospace Engineering Department, University of California, San Diego, La Jolla, USA.

Corresponding author: S. Sarkar, Mechanical and Aerospace Engineering Department, University of California, San Diego, 9500 Gilman Dr., La Jolla, CA 92094, USA. (sarkar@ucsd.edu)

ocean pycnocline. *Martin et al.* [2006] observed clustering of energy surrounding the ray path of the beam extending up to  $\sim 50$  km from the topography before it hits the upper surface. There was no such energy clustering below the pycnocline in the reflected wave beam path. Another set of observations of the across-ridge structure of internal tides has been obtained at Kauai Channel by *Cole et al.* [2009] using SeaSoar and a Doppler sonar over the upper 400–600 m of the ocean extending 152 km on each side of the ridge. The pycnocline thickness was approximately 125 m, and the internal wave beam shear below the pycnocline shows high modes with a vertical thickness that is 50 m and smaller. *Cole et al.* [2009] clearly identified upward propagating internal wave beams emanating from the two sides of the ridge in the velocity variance signal; however, a clear beam signature was absent in the reflected downward-propagating wave signal below the pycnocline. Downward-propagating beams in velocity shear (a measurement that is biased toward higher vertical modes) were even more difficult to identify. The structure of the internal wave beams in the same site was examined over a larger water depth by *Pickering and Alford* [2012], who utilized acoustic Doppler current profiler data that extended to 1000–1500 m. Although the M2 component dominated, *Pickering and Alford* [2012] found features with a shallower slope in the pycnocline with slope close to K2 internal tide or (1/2)M2 subharmonic waves. Seismic reflection maps provide striking images of high-mode wave structure. A seismic reflection image extending over hundreds of meters vertically and tens of kilometers laterally in the Norwegian Sea [*Holbrook et al.*, 2009] detected high-mode IW beams and showed fine-scale structures inside the seasonal pycnocline between 300 m and 700 m, particularly in the proximity of the IW beam ray paths.

[5] The formation of subharmonics during the interaction of an IW beam with an upper ocean pycnocline has not been previously identified. However, recent numerical and field studies have found evidence of direct energy transfer from M2 to (1/2)M2 frequency by PSI in other situations. *Rainville and Pinkel* [2006] measured a subharmonic signal in upper ocean velocity and displacement data in the near field and the far field (450 km offshore) of a strong internal tide generation site at Kaena Ridge during the Hawaii Ocean Mixing Experiment (HOME). In the far field, independent of any diurnal forcing, the energy flux associated with diurnal frequency varies in accord with the fortnightly cycle of the barotropic semidiurnal tide, suggesting direct energy transfer from the M2 internal tide to internal waves at frequencies (1/2)M2. *Carter and Gregg* [2006], based on 1 month data from a deep-profiling shipboard Doppler sonar, observed cross-frequency energy transfer in a narrow depth range (525–595 m) from the M2 tide to the (1/2)M2 frequency in an IW wave beam close to Kaena Ridge. A recent study by *Sun and Pinkel* [2013] used bispectral analysis to examine data collected by FLIP's (FLoating Instrument Platform) vertical profiler that intersected a southward traveling internal tide emanating from Kaena Ridge. Significant energy transfer was found from the low-mode M2 internal tide to subharmonics with frequency near (1/2)M2 and vertical wavelengths of  $O(120$  m).

[6] The numerical experiments of *Hibiya et al.* [2002] and *MacKinnon and Winters* [2005] show that a significant

amount of energy is transferred to (1/2)M2 from M2 by nonlinear interactions for plane monochromatic waves near the critical latitude ( $\lambda_c = 28.9^\circ\text{N}$ ) leading to potentially catastrophic breakdown of the M2 tide. The observations of *Alford et al.* [2007] indicate intense, vertically standing, near-inertial waves near the critical latitude that suggest PSI; however, there was no significant loss in the M2 tidal energy flux. *Hazewinkel and Winters* [2011], using numerical simulations, attribute the absence of catastrophic breakdown of the M2 tide to the time scale of the PSI being of the same order as the spring-neap cycle, thus disallowing sufficient time for explosive growth of PSI. *MacKinnon et al.* [2013] examined observations of the rather complex oceanic IW environment to deduce that, near  $\lambda_c$ , there is a statistically bicoherent phase between the internal tide and upward/downward near-inertial waves that leads to positive energy transfer from the M2 internal tide to the near-inertial waves. *Gerkema et al.* [2006] in their numerical experiments showed breaking of an IW beam close to the supercritical topography. Radiation of subtidal beam-like structures, along with the fundamental beam, are observed in recent simulations of an ocean ridge [*Korobov and Lamb*, 2008] and continental slope [*Gayen and Sarkar*, 2010] during the generation of internal tides.

[7] Internal wave beams may also interact with the pycnocline to locally generate internal solitary waves (ISWs) that are groups of horizontally propagating interfacial gravity waves. Although ISWs have not been noted in the aforementioned observational studies at the Hawaiian ridge, mode-1 ISWs observed in the Bay of Biscay have been attributed to IW beam/pycnocline interaction [*New and Pingree*, 1992]. *Gerkema* [2001] using theory and numerical modeling found the mode-1 ISW formation to be controlled by the parameter  $\gamma = c_p/N_1H$  with the most energetic ISWs occurring when  $\gamma \sim 0.12$ . Here,  $c_p$  is the interfacial phase speed based on a two-layer approximation calculated using the relative density difference across the pycnocline and vertical depth of the center of the pycnocline from the top surface.  $N_1$  is the buoyancy frequency of the bottom layer and  $H$  is the depth of the ocean. *Akylas et al.* [2007] introduced another controlling parameter  $\alpha = N_1\lambda_0/c_p$  (where  $\lambda_0$  is the transverse wavelength of the beam) for generation of ISW at the interface of a two-layer ocean of infinite depth and showed maximum interfacial displacement at  $\alpha \sim 1$ .

[8] *Mathur and Peacock* [2009] have performed a set of laboratory experiments on the propagation of both plane IW and localized IW beams through variable density interfaces. Their laboratory experiments, limited to the laminar regime, indicate that nonuniform stratification disrupts a beam, ducts energy, and affects beam transmission and reflection. Subsequent numerical [*Grisouard et al.*, 2011] and experimental [*Mercier et al.*, 2012] studies with parameters tuned to the ISW regime found mode-1 ISWs when the parameter  $\gamma \simeq 0.1$ , consistent with the criterion advanced by *Gerkema* [2001]. *Mercier et al.* [2012] also observed a mean flow, generated in the direction of wave propagation. Numerical process studies have generally assumed a uniform stratification; therefore, beam structure is maintained after surface and bottom reflections. A notable exception is the analytical/numerical work of *Grisouard et al.* [2011], where a beam incident on the thermocline is

**Table 1.** Simulation Parameters<sup>a</sup>

Physical Parameters		A1	A2	A3	A4	A5
Vertical thickness of IW beam	$l_b$ (m)	100	100	100	100	100
Vertical thickness of pycnocline	$l_{py}$ (m)	85	50	25	10	50
Relative thickness of IW beam	$l_b/l_{py}$	1.2	2	4	10	2
Velocity of IW beam	$u_0$ (cm/s)	0.1	0.1	0.1	0.1	0.41
Frequency of IW beam	$\Omega$ (s <sup>-1</sup> )	$1.4 \times 10^{-4}$	–	–	–	–
Froude number	$Fr = u_0/(N_1 l_b)$	0.035	0.035	0.035	0.035	0.035
Deep stratification	$N_1$ (s <sup>-1</sup> )	$2.8 \times 10^{-4}$	–	–	–	$1.15 \times 10^{-3}$
Pycnocline inhomogeneity	$\Gamma = N_2/N_1$	4	4	4	4	4
Incoming IW angle	$\theta$ (°)	30	30	30	30	7
ISW criterion, <i>Gerkema</i> [2001]	$\Gamma$	1.095	0.704	0.476	0.405	0.5
ISW criterion, <i>Akylas et al.</i> [2007]	A	0.165	0.258	0.381	0.448	0.414
Remark		PSI	PSI	PSI	Negligible PSI	PSI

<sup>a</sup>In cases A1–A4, the thickness of the pycnocline is progressively decreased relative to the incident beam width. Case A5 has a shallower beam angle of 7° that is closer to oceanic conditions.

investigated using two-dimensional simulation of the Navier-Stokes equations accomplished with the MIT-gcm. Higher harmonics trapped in the pycnocline and internal solitary waves (ISWs) of mode 1 were found. Mode-2 and mode-3 ISWs were also found to occur when the parameters were such that the interfacial phase speed matches with wave speeds of higher modes in the water column.

[9] In order to study the interaction of an internal wave beam with an upper ocean pycnocline, we performed numerical simulations using our nonhydrostatic computational model [Gayen and Sarkar, 2011b]. The physical parameters used in the present study place the simulations in a different parameter regime with respect to optimal ISW generation. For instance, cases A1–A5 in Table 1 have  $\gamma$  larger than the  $\gamma = 0.12$  criterion and  $\alpha$  smaller than the  $\alpha = 1$  criterion. Correspondingly, ISWs that are found here do not constitute the prominent feature of the flow evolution but become larger in amplitude progressively from case A1 to case A4. On the other hand, the degradation of the incoming beam during its interaction with the pycnocline by PSI is the dominant feature except for case A4, as will be discussed later.

## 2. Problem Formulation

[10] A linear, two-dimensional wave beam propagates upward in a thermally stratified medium of constant density gradient,  $N_1$ . It then encounters the upper ocean with a continuously varying density gradient in the vertical direction,  $z$ : a mixed layer on top of a pycnocline of strength  $N_2$ . The pycnocline layer has a thickness,  $l_{py}$  (denoted in Figure 1 for case A1), which is varied in a parametric study.

[11] In the present study, five cases are simulated with parameters as listed in Table 1. For all cases, the incoming beam frequency is  $\Omega = 1.4076 \times 10^{-4}$  rad s<sup>-1</sup> and  $T = 2\pi/\Omega = 12.4$ h, which corresponds to the diurnal M2 tide period. Internal tidal beams generated by bottom ocean topography often have a shallow propagation angle of  $\theta \sim 2$ –7°. It is computationally very expensive to model such a shallow beam with the small grid size required to meet our objective of high-resolution simulations because it covers a large streamwise domain length, requiring a significantly large number of grid points in the horizontal direction. Therefore, the parametric study of the influence of the ratio of beam thickness to pycnocline thickness,  $l_b/l_{py}$ , performed in cases A1–A4, utilizes a steeper angle of 30°. In contrast,

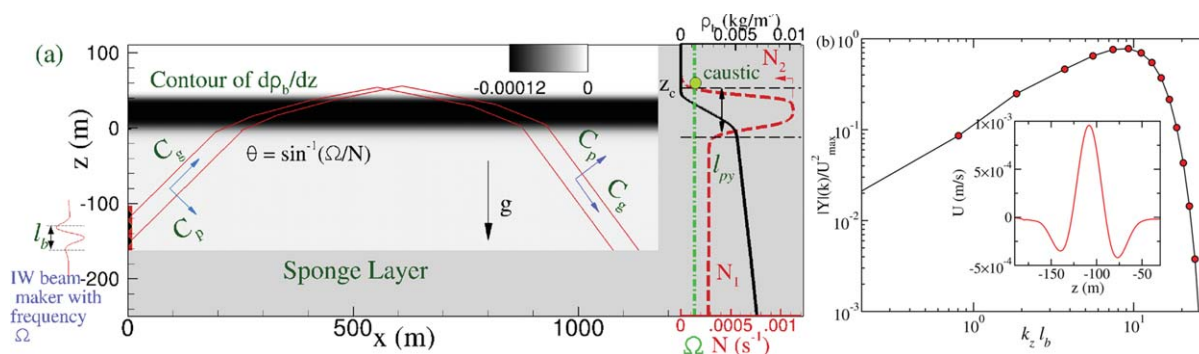


**Figure 1.** (a) Schematic of the problem along with internal wave beam maker at the left side and sponge region at the right and bottom of the computational domain. IW beam path is denoted by red line. Background color shade in the figure indicates the stable density gradient. Profiles on the right correspond to background density,  $\rho_b(z)$ , and buoyancy profile,  $N(z)$ , where  $N_1$  and  $N_2$  are the buoyancy frequency in the lower part of the domain and at the pycnocline center, respectively. (b) Nondimensional power spectrum of the horizontal velocity in the beam. Inset shows the vertical profile of horizontal velocity at the left side domain boundary corresponding to the incoming beam.

case A5 has a shallower angle of  $7^\circ$ , closer to oceanic values, and is simulated to verify that the PSI found in cases A1–A4 is robust to the choice of wave propagation angle. For cases A1–A4, the lower ocean background buoyancy frequency is set to  $N_1 = 2.8152 \times 10^{-4} \text{ rad s}^{-1}$ , a value smaller than typical, which gives an incoming wave angle  $\theta = \sin^{-1}(\Omega/N_\infty) \approx 30^\circ$ . The strength of the density change in the pycnocline is  $\Gamma = N_2/N_1 = 4$ . The pycnocline thickness,  $l_{py}$  is 100 m for case A1 and decreases to 10 m for case A4. The kinematic viscosity,  $\nu = 10^{-6} \text{ m}^2/\text{s}$ , is that of water with Prandtl number  $Pr = 7$ . The beam width in the vertical direction is  $l_b = 100 \text{ m}$ , which is consistent with the vertical width of the internal wave shear regions in the beams observed off Kaena Ridge. In cases A1–A4, the velocity amplitude is chosen to be  $u_0 = 0.1 \text{ cm/s}$ , a value that is substantially smaller than in the HOME near-field measurements. We choose a small wave velocity to compensate for the lower value of  $N_1$  chosen here, in order that the Froude number of the incoming beam based on  $u_0$ ,  $N_1$ , and  $l_b$  is  $Fr = u_0/(N_1 l_b) = 0.035$ , a moderate value that is guided by oceanic examples. Case A5 has an incoming wave angle,  $\theta = 7^\circ$ , that was chosen to be closer to typical oceanic values of wave propagation angle, and the corresponding value of  $N_1 = 1.155 \times 10^{-3} \text{ rad s}^{-1}$  is also closer to mid-ocean stratification. The beam velocity amplitude is chosen for this case to be  $u_0 = 0.41 \text{ cm/s}$  so that  $Fr$  is identical to the other cases. The effects of Earth's rotation are not included. Rotational effects will modify but not change the existence of resonant triads during the interaction process.

[12] Our computational model [Gayen and Sarkar, 2011b] was employed in a two-dimensional mode and without recourse to subgrid models. The full NS equations (including nonhydrostatic effects) are numerically solved to obtain the velocity  $[u, w]$  and the deviations from background density and pressure as a function of Cartesian coordinates  $[x, z]$ . Spanwise derivatives are treated with a pseudospectral method and other derivatives with second-order finite differences. A low-storage, third-order Runge-Kutta-Wray method is used for time stepping, except viscous terms, which are treated implicitly with the alternating direction implicit method. Pressure correction is done by a fractional step method. For cases A1–A4, the test domain, excluding the sponge region, consists of a rectangular box of 1200 m length and 300 m height. The grid size in the test domain is  $890 \times 500$  in the  $x$  and  $z$  directions, respectively, with stretching in both directions. In case A5, the box has length of 3200 m and a height of 300 m with resolution of  $2300 \times 500$  points in the  $x$  and  $z$  directions, respectively. The grid spacing ( $\Delta x_{min} = 0.5 \text{ m}$ ,  $\Delta x_{max} = 1.2 \text{ m}$ ,  $\Delta z_{min} = 0.25 \text{ m}$ ,  $\Delta z_{max} = 1 \text{ m}$ ) is sufficient to resolve smaller waves created during the subharmonic instability. Variable time stepping with a fixed Courant-Friedrichs-Lewy number of 1.2 is used leading to  $\Delta t \simeq \mathcal{O}(1) \text{ s}$ . Although not spatially three-dimensional, each simulation is computationally expensive because of the small  $\Delta t$ , since one tidal cycle (approximately 50,000 time steps) takes approximately 1000 CPU hours to simulate.

[13] The flow is forced at the left side of the computational domain based on the analytical value of the parallel and transverse velocity components, as well as the buoyancy fields of the Thomas-Stevenson profiles [Thomas and

Stevenson, 1972; Mercier et al., 2010]. The profiles constitute a viscous, self-similar solution of the Navier-Stokes equations and have zero integrated mass flux. For given environmental parameters (viscosity, buoyancy frequency, and wave forcing frequency), there is a free parameter that sets the beam width,  $l_b$ , at  $x = 0$ . The energy in the internal wave beam spans a broad range of wave numbers as shown by the power spectrum of the streamwise velocity in Figure 1b obtained from data taken on vertical sections of the incident IW beam. At the top of the domain, a free surface condition with the rigid-lid approximation is imposed with zero gradient value for the density. The right and bottom boundaries are artificial boundaries corresponding to the truncation of the domain. Rayleigh damping or a sponge layer is used at the right and the bottom of computational domain, shown in Figure 1, so as to minimize spurious reflections from the artificial boundary into the test section of the computational domain. The sponge region for cases A1–A4 at the right boundary contains 25 points and extends from 1200 to 1500 m, while the bottom sponge with 15 points extends from  $z = -180$  to  $-250 \text{ m}$ . The strength of the sponge region was adjusted until reflection from the internal wave beams incident on the sponge was found to be negligible.

### 3. Results: Case A1

[14] After entering from the left boundary, an internal wave beam arrives at the upper pycnocline in approximately 2 days. The beam thickness is close to the thickness of the pycnocline. As time progresses, various nonlinear phenomena take place, such as formation of harmonics and resonant subharmonic instability, as will be explained below.

[15] Figure 2 illustrates the evolution of the horizontal velocity field by showing snapshots in the  $x$ - $z$  plane at three different times. An internal wave beam, after entering the domain from the left hand side at  $z \sim -130 \text{ m}$ , travels into the pycnocline at  $z = -15 \text{ m}$ . During transmission through the lower transition layer,  $N_1 \rightarrow N_2$  of the pycnocline, the beam narrows owing to enhancement of the vertical wave number, as governed by

$$m^2(z) = k^2 \left[ \frac{N^2(z)}{\Omega^2} - 1 \right], \quad (1)$$

and also refracts, i.e., bends toward the horizontal owing to increasing stratification. In the upper portion of the pycnocline ( $N_2 \rightarrow 0$ ), the internal wave beam becomes steeper owing to a decrease of the stratification and the vertical length scale increases ( $m$  decreases) as it approaches the caustic  $z = z_c$  according to equation (1). Maximum amplification of the vertical wave velocity occurs slightly below the caustic and decreases exponentially above it. Later, after being reflected from the caustic, the IW beam returns back to the bottom medium through the transition layer. Prior to time  $t \simeq 10T$ , the wave behavior is linear. As time progresses, higher harmonics ( $\omega = n\Omega$ ,  $n \in \mathbb{N}$ ) originate in the reflected beam at  $x \sim 580 \text{ m}$ . A remarkably complex wave pattern associated with the reflected beam is shown in Figure 2b. The wave at the second harmonic ( $2\Omega$ ) that propagates down inside the pycnocline is clearly visible.

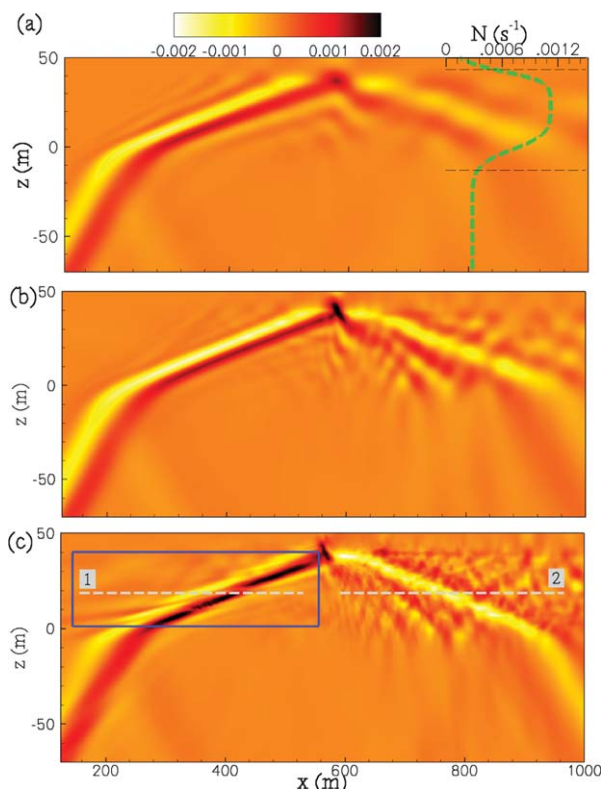


**Figure 2.** Overview of simulated IW beam dynamics during the interaction of an internal wave beam that propagates upward from the lower left corner, with the upper ocean pycnocline. Streamwise ( $x$  direction) velocity (m/s) contours are shown at different times: (a) laminar response at  $t=10T$ , buoyancy profile of the background shown in green; (b) weakly nonlinear regime with trapped higher harmonics in the region at  $t=15T$ ; (c) nonlinear response exhibiting the formation of subharmonics in the incident region (marked with the box) of the beam at  $t=18T$ . All snapshots are taken at the same phase.

Since the harmonics have frequencies that do not allow propagation in deep water, they reflect back from the lower transition layer  $N_2 \rightarrow N_1$  at  $x \sim 780$  m. There is a similar reflection from their corresponding caustic ( $N=2\Omega$ ) at  $x \sim 950$  m. This process continues and repeats for other higher harmonics, resulting in the trapping of higher harmonics inside the pycnocline similar to recent numerical [Grisouard *et al.*, 2011] and experimental [Mercier *et al.*, 2012] studies at laboratory scale.

### 3.1. Identification of Parametric Subharmonic Instability (PSI)

[16] As time progresses, the incoming internal wave field becomes more complex inside the pycnocline owing to parametric subharmonic instability (PSI). During this process, the incoming beam is distorted in the pycnocline due to the superposition of newly formed subharmonic waves, which have shallower characteristic angles compared with the fundamental beam, as shown in the boxed region of Figure 2c. The subharmonic waves with negative group velocity encounter the left domain boundary where a sponge is placed to absorb the waves. This sponge has a strength

that linearly decreases from a maximum at  $z=150$  m to zero at  $z=0.0$  m, well above the wavemaker. The formation of the subharmonic waves is associated with refraction of the internal wave beam as it travels from the bottom region with buoyancy frequency  $N_1$  through the pycnocline with increased stratification,  $N_2$ . Simulations of beam propagation through a uniformly stratified medium (either  $N_1$  or  $N_2$ ) or beam reflection at a rigid boundary do not show the instability leading to subharmonics.

[17] To analyze the energy transfer among the higher harmonics and the subharmonics, we have calculated the spectrogram  $\mathcal{Y}(\omega, t)$ , which represents the temporal evolution of the spectrum  $Y(\omega)$ . The spectrum at a given time is calculated using a time window centered at that time and chosen to be  $10T$  to accurately capture internal wave signals at lower frequency. Figure 3a shows that, before  $t=120$  h, the velocity field of the incident wave has a dominant peak at the frequency,  $\omega_0 = \Omega$ , where  $\Omega$  is the tidal M2 frequency. Soon after, the spectrum reveals two additional peaks,  $\omega_1 \sim 0.3 \Omega$  and  $\omega_2 \sim 0.7 \Omega$ , in the subharmonic regime  $(0, \Omega]$ . The corresponding effect on the spatial structure of the incident beam was earlier noted in Figure 2c. The two newborn wave packets together with the forced internal wave beam constitute a resonant triad ( $\omega_1 + \omega_2 = \omega_0$ ) and, by gaining energy from the forcing IW beam of frequency  $\omega_0$ , weaken the main wave beam. A noticeable difference in the spectra is found in the reflected beam as shown in Figure 3b. High harmonics ( $n\Omega, n \in \mathbb{N}$ ) of the tidal frequency are seen instead of subharmonics.

[18] We now turn to the description of the triad interaction in wave number space by processing the data with band-pass filters corresponding to the participating frequencies. During the initial period before  $t=180$  h, the original unfiltered data shown in Figure 4a exhibit phase lines that are well organized and inclined toward the right, indicating positive horizontal wave number and rightward phase propagation. Figure 4a shows that, soon after  $t=180$  h, the incident wave beam experiences subharmonic instability, forming additional internal wave packets with different phase angles and frequencies including leftward propagation. The data, band-passed into the forcing frequency ( $\omega_0 \sim 0.95 - 1.05\Omega$ ) and plotted in Figure 4b, show the forcing IW wave field with a rightward inclined phase over the entire time span. The dominant wave number,  $k_x$ , for a given signal is obtained by using the slope of the  $x$ - $t$  curves to infer the phase speed,  $C_{px}$ , and then using  $\omega = C_{px}k_x$ . The dominant horizontal wave number of the incident beam is  $k_{x,0} \simeq 0.06 \text{ m}^{-1}$ . Space-time diagrams of the two IW wave packets after band passing around  $\omega = 0.7 \Omega$  and  $\omega = 0.3 \Omega$  are shown in Figures 4c and 4d, respectively. The internal wave with frequency  $\omega \sim 0.7 \Omega$  has smaller phase speed and a larger wave number magnitude ( $k_{x,1} \sim 0.09 \text{ m}^{-1}$ ) compared with the main beam. We emphasize that the smallest horizontal scale ( $l_x \sim 78.5$  m) of the wave produced during PSI is well resolved with the existing grid resolution in the horizontal direction. The IW having frequency  $\omega = 0.3 \Omega$  exhibits phase lines in the  $x$ - $t$  plane that are oriented leftward, which is consistent with negative phase velocity, as was also evident in the spatial structure of the incident beam in Figure 2c. This wave has a wave number  $k_{x,2} \sim -0.03 \text{ m}^{-1}$  showing a resonant triad condition, i.e.,  $k_{x,0} = k_{x,1} + k_{x,2}$ .

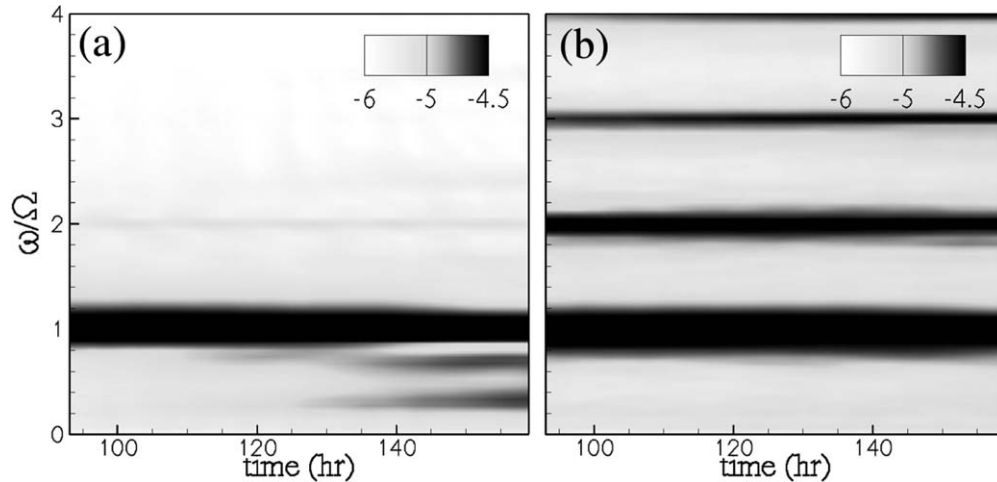


**Figure 3.** Evolution of the line averaged spectrum,  $\langle \mathcal{Y} \rangle(\omega, t)$ , of streamwise beam velocity measured inside the pycnocline. (a and b) Correspond to data measured at the horizontal lines indicated by the dashed lines 1 (incident beam) and 2 (reflected beam), respectively, in Figure 2c. The incident beam in Figure 2a shows the fundamental frequency as a dark black horizontal band and the two subharmonics as two gray horizontal bands starting at  $t \sim 110$  h and progressively darkening with increasing time. The reflected beam in Figure 2b, on the other hand, shows only horizontal bands corresponding to higher harmonics in addition to the fundamental.

[19] The resonant triad condition is also satisfied by the vertical wave numbers. Analogous to the calculation of the horizontal wave numbers discussed above, the vertical phase speeds,  $C_{pz}$ , are obtained from the  $z$ - $t$  diagrams (Figure 4, bottom part) of data band-passed at the three participating frequencies followed by calculation of  $k_z$ . For the present case,  $k_{z,0}(-0.4 \text{ m}^{-1})$ ,  $k_{z,1}(-0.92 \text{ m}^{-1})$ , and  $k_{z,2}(0.52 \text{ m}^{-1})$  participate in the PSI.

[20] The triad in the resonant instability found here involves  $\omega_0 = \Omega$ ,  $\omega_1 = 0.7 \Omega$ , and  $\omega_2 = 0.3 \Omega$ , not the values of  $\omega_1 = \omega_2 = 0.5 \Omega$  often associated with PSI. In the present simulations, there is growth in the energy at  $0.5 \Omega$ , but it is small relative to the resonant subharmonics. As will be discussed later, case A5 with higher stratification and shallower beam angle of  $7^\circ$  exhibits PSI with subharmonic frequency of approximately  $0.5 \Omega$ . Subharmonic instability involving

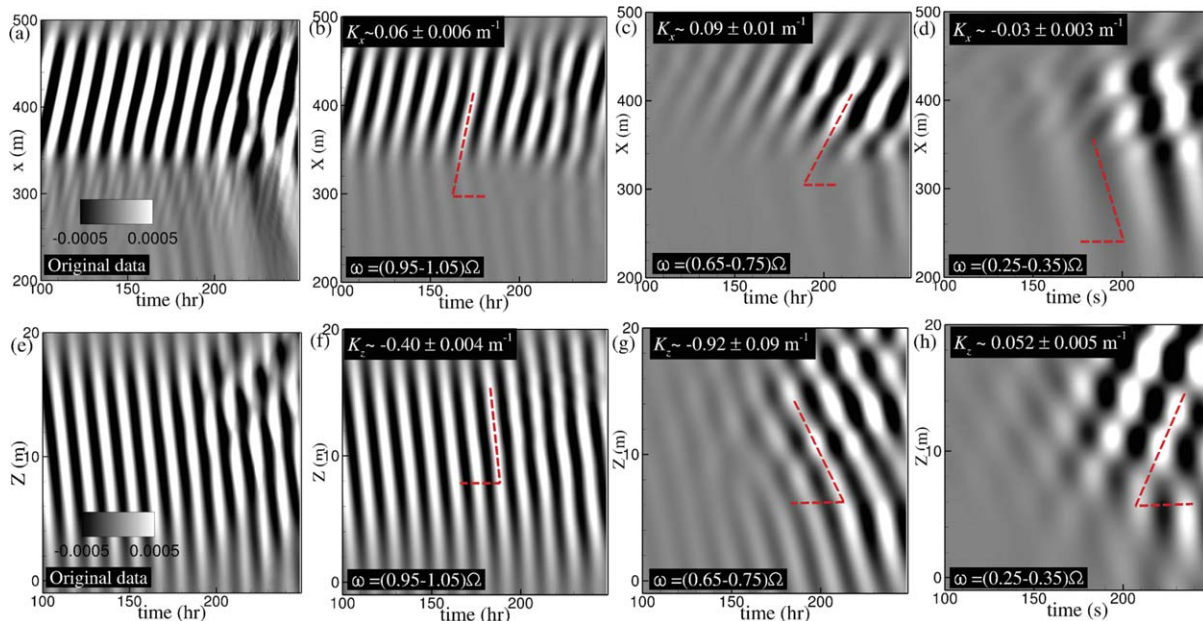


**Figure 4.** Time series of horizontal velocity (m/s) along a line of original data and band-passed in time frequency ranges, as indicated at the bottom left of each plot. The beam incident in the pycnocline (data on line 1 in Figure 2c) is considered here. (top)  $x$ - $t$  plots corresponding to data on a horizontal line and (bottom)  $z$ - $t$  plots corresponding to data on a vertical line,  $x = 400$  m.

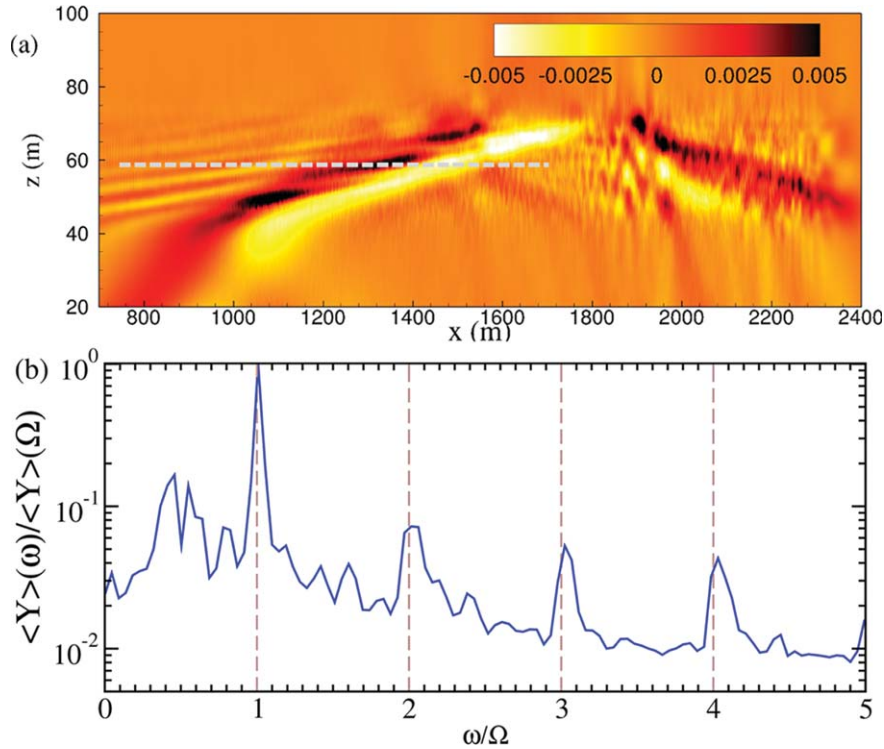


**Figure 5.** (a) Overview of simulated IW beam dynamics for case A5 during the interaction with the upper ocean pycnocline shown by streamwise velocity contours at  $t = 25T$ . Here,  $T$  is the time period  $2\pi/\Omega$ . (b) Line-averaged power spectrum  $\langle Y \rangle(\omega) / \langle Y \rangle(\Omega)$  of streamwise beam velocity measured inside the pycnocline. The time series is taken over  $20T$ . Numerical data taken at the horizontal line is indicated in Figure 5a.

waves with unequal frequencies has been found previously [Korobov and Lamb, 2008; Bourget et al., 2013] but not in the ocean to the best of our knowledge. Bourget et al. [2013] show analytically that, at a low Reynolds number, the fastest growing instability corresponds to unequal frequencies of the daughter waves, thus explaining their laboratory findings. Cases A1–A4 have a Reynolds number,  $Re_b = u_0 l_b / \nu$ , that is 2 orders of magnitude below the oceanic value, which may lead to the unequal frequencies of the most unstable waves found here. In general, the selection of daughter wave frequency/wave number combinations depends on the properties of the incoming beam such as frequency, wave number spectra, and Reynolds number.

[21] Waves of a smaller length scale, originating from PSI, may be susceptible to convective overturning. Density profiles (not shown) at a late time indicate a density inversion with a negative value of  $Ri_g$  around  $z \sim 7$  m. Simulations are terminated after  $t = 20T$  because the present two-dimensional grid is not adequate to resolve the three-dimensional fine-scale turbulence and to measure the dissipation accurately. Turbulence dynamics, whose simulation will require large eddy simulation (LES), will be the subject of a future investigation.

#### 4. Interaction of an IW Beam at a Shallow Angle ( $7^\circ$ ) With the Pycnocline

[22] In cases A1–A4, the IW propagation angle was chosen to be  $\theta = 30^\circ$ . In reality, such a steep beam angle is not

common in the ocean. As noted earlier, it is computationally very expensive to model a shallow beam because it necessitates a significantly large number of grid points in the horizontal direction. Therefore, rather than performing a parametric study with a shallow beam angle, we simulate a single additional case with more realistic stratification in order to verify that the finding of PSI holds for shallow beams. Case A5 has a bottom buoyancy frequency of  $N_1 = 1.155 \times 10^{-3} \text{ rad s}^{-1}$  corresponding to a beam angle of  $\theta = 7^\circ$ . The velocity amplitude of the incoming beam is  $u_0 = 0.41 \text{ cm/s}$ , which leads to  $Fr = 0.035$ , identical to the other simulated cases. Similar to cases A1–A3, PSI is found to disintegrate the incident beam in case A5 as shown in Figure 5a.

[23] Figure 5b shows the power spectrum of horizontal velocity inside the pycnocline. The two energy peaks, found to occur at subharmonics of  $\omega \sim 0.3 \Omega$  and  $\omega \sim 0.7 \Omega$  in cases A1–A3, shift very close to  $\omega \sim 0.5 \Omega$  in the present case A5. The spectrum also shows several temporal harmonics ( $n\Omega, n \in \mathbb{N}$ ) in the IW beam even before reflection. The incident beam has a spectral peak at  $k_{x,0} = 0.012 \pm 0.001 \text{ m}^{-1}$  and  $k_{z,0} = -0.29 \pm 0.03 \text{ m}^{-1}$ . From space-time data after band passing at  $0.5\Omega \pm 0.05\Omega$ , the horizontal wave numbers of the subharmonic waves participating in PSI are found to be  $k_{x,1} \simeq -k_{x,2} = 0.06 \pm 0.006 \text{ m}^{-1}$  and the corresponding vertical wave numbers are  $k_{z,1} \simeq -k_{z,2} = -2.9 \pm 0.3 \text{ m}^{-1}$ . Consistent with the theory of PSI involving  $\omega_0$  and  $\omega_0/2$ , the wave number components of the subharmonic are much larger than those of the primary wave.

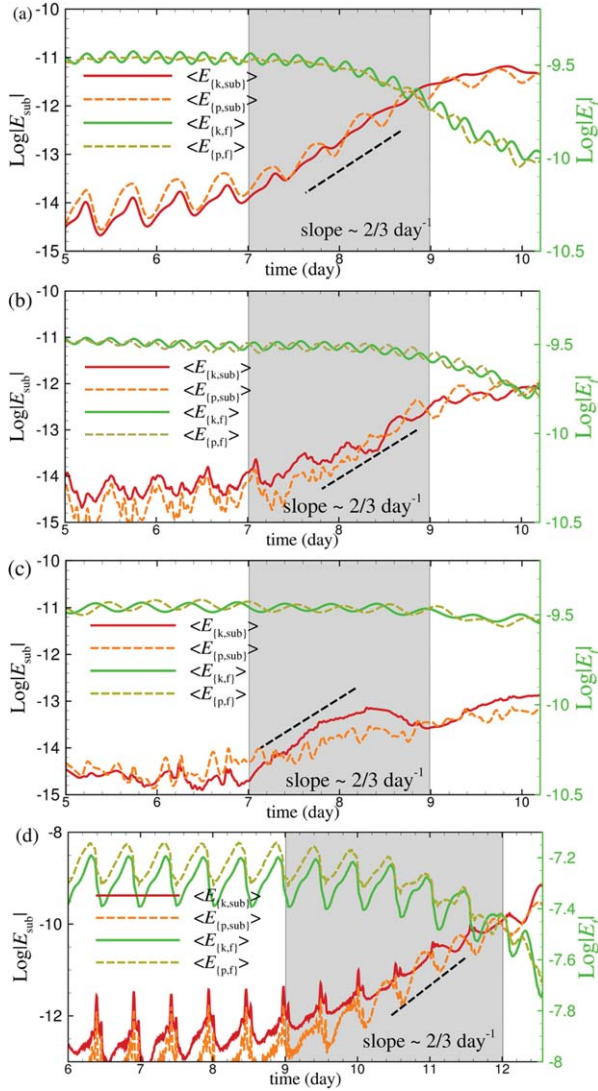


**Figure 6.** Evolution of the fundamental and subharmonic wave energy for cases A1, A2, A3, and A5 are shown in Figures 6a–6d, respectively. Area averaged kinetic energy,  $\langle E_{k,sub} \rangle$ , (solid red line) and potential energy  $\langle E_{p,sub} \rangle$  (dashed orange line) of the subharmonic wave motion as function of day. Corresponding quantities for the fundamental tidal frequency are also shown. The area of integration for cases A1–A3 is marked by a rectangle in Figure 2c.

## 5. Energetics of PSI

[24] Energy is transferred from the fundamental to the subharmonics during PSI. This process is quantified, and the dependence of the energy transfer on the thickness of the pycnocline relative to that of the beam is assessed. The area-averaged kinetic energy,  $\langle E_{k,sub} \rangle = 1/2 \rho_0 \langle \mathbf{u}_{sub} \cdot \mathbf{u}_{sub} \rangle$  and potential energy  $\langle E_{p,sub} \rangle = 1/(2\rho_0) (g\rho_{sub}^*/N)^2$  of the two subharmonic modes is calculated and plotted in Figure 6. Note that after computing the two subharmonic components by spectral filtering of the simulation data, the energies in each subharmonic are added and the sum plotted as  $E_{k,sub}$  and  $E_{p,sub}$ . For case A1, the growth is negligible during the initial 7 days. During the time interval,  $\Delta t \sim 7 - 9.5$  days,

the subharmonic energy grows exponentially with a growth rate of

$$\sigma_t = \frac{1}{\langle E_{sub} \rangle} \frac{d\langle E_{sub} \rangle}{dt} \simeq 2/3 \text{ per day}. \quad (2)$$

[25] The area-averaged kinetic energy,  $\langle E_{k,f} \rangle$ , and potential energy,  $\langle E_{p,f} \rangle$ , associated with the M2 wave beam are also shown. In response to PSI, which transfers energy to the subharmonic motions, both the kinetic and the potential energy of the main beam drop after  $t \simeq 7$  days. Cases A2 and A3 with thinner pycnoclines also show PSI with the same growth rate. However, with decreasing pycnocline width, the amount of energy transfer to the subharmonic drops significantly. For the thinnest pycnocline ( $l_{py}/l_b = 0.1$ ), the energy transfer is almost negligible (not shown here). Case A5 (beam with shallower angle of  $7^\circ$ ), whose wave energetics is shown in Figure 6d, exhibits exponential growth with a rate of approximately two-thirds per day, similar to cases A1–A3.

[26] The reason for the absence of PSI in case A4 is as follows. The wave with frequency  $\omega \sim 0.7 \Omega$  has wave number of  $k_{z,1} \sim 0.92 \text{ m}^{-1}$  corresponding to a wavelength of  $\lambda_{z,1} \sim 6.8 \text{ m}$ . The distance over which the buoyancy frequency changes from  $N_1$  to its peak,  $N_2$ , is  $l_{py}/2$ , and the subharmonic waves are established within this region in cases A1–A3. However, case A4 has  $l_{py}/2 = 5 \text{ m}$ , which is smaller than the wavelength,  $\lambda_{z,1} \sim 6.8 \text{ m}$ . Since the thin pycnocline of case A4 does not satisfy the constraint,  $l_{py}/2 > \lambda_{z,1}$ , where  $\lambda_{z,1}$  is the smallest vertical wavelength of the wave triad, PSI is not effective in removing energy from the incoming beam.

## 5.1. Three-Dimensional Simulations

[27] The dynamics discussed here are two-dimensional. Nevertheless, we perform a three-dimensional simulation in order to confirm that allowing for the third dimension does not change the primary result of the paper, i.e., beam

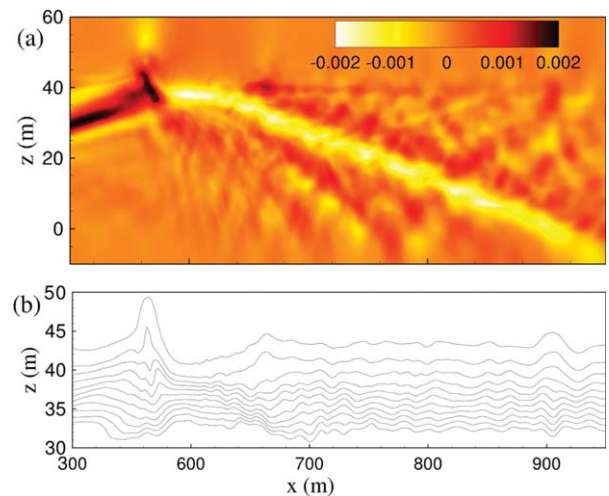


**Figure 7.** A zoomed region of Figure 2c corresponding to case A1 that shows behavior at a particular time within the pycnocline after the main beam hits the interface with the upper mixed layer: (a) streamwise velocity (m/s) and (b) isopycnals.

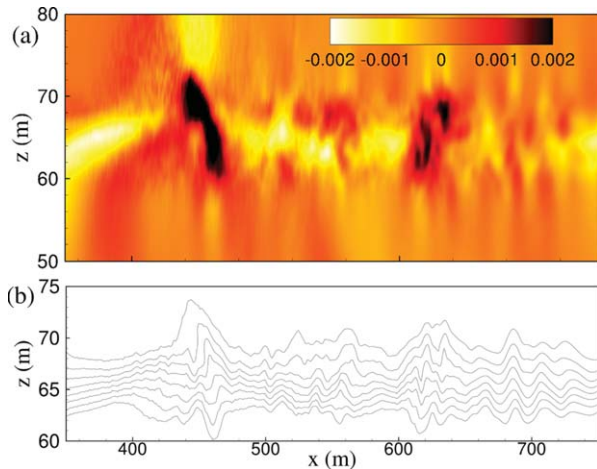


**Figure 8.** Zoomed region of the pycnocline for case A4 at a particular time: (a) streamwise velocity and (b) isopycnals.

degradation. Case A1 was rerun with 20 m width in the spanwise  $y$  direction and  $\Delta_y = 0.3$  m. Comparison of the energy evolution (plot not shown) with the corresponding evolution in the 2-D simulation shown in Figure 6a shows little difference. At late time (not shown here), there are convective overturns and growth of small-scale turbulence that cannot be resolved by the grid employed here and will have to await a future large eddy simulation (LES).

## 6. Internal Solitary Wave (ISW)

[28] The values of  $\gamma$  and  $\alpha$ , parameters that were defined in the introduction, do not satisfy the optimal criteria for ISWs with case A1 being furthest away and case A4 being closest to the optimal criteria of  $\gamma = 0.12$  and  $\alpha = 1$ . Figure 7 shows a zoomed view of Figure 2c corresponding to case A1 to illustrate the behavior within the pycnocline. The interface with the mixed layer shows a large deformation at  $x \sim 550$  m where the main beam is incident. There are other deformations of the interface at larger  $x$ . These deformations occur owing to reflection of higher harmonics at the interface as well as ISWs. For instance, the deformation at  $x = 670$  m corresponds to a mode-2 ISW and that at  $x = 900$  m corresponds to a reflected second harmonic. Figure 8 is a corresponding figure for case A4. This case has the largest value of beam thickness with respect to the pycnocline thickness,  $l_b/l_{py} = 10$ , and does not exhibit PSI. Interfacial displacements by mode-2 and mode-1 ISWs are clearly present in case A4 and have a larger amplitude than in case A1.

## 7. Conclusion

[29] The interaction of an internal tide beam with an upper ocean pycnocline has been examined using numerical simulation. The fine grid utilized here allows a space-time description of small-scale waves during the interaction. The incident beam is found to exhibit a strong nonlinear response, driven by parametric subharmonic instability (PSI), as it travels upward through the increasing stratification of the pycnocline. Diagnostics applied to the numerical

data show the development of subharmonics that form a resonant triad. During the PSI, energy transfer occurs to subharmonic motions, leaving a weaker incident wave beam. Beam degradation owing to PSI is found here when the beam thickness,  $l_b$ , is not too large, i.e., does not exceed the pycnocline thickness by an order of magnitude or more. Case A4, with the thickest beam ( $l_b/l_{py} = 10$ ) considered here, does not result in beam degradation because of insufficient space in the pycnocline for PSI to develop; in particular, the vertical wavelength of the shortest wave of the resonant triad is larger than the distance over which the buoyancy frequency in the pycnocline increases from a uniform value to its peak. On the other hand, the generation of internal solitary waves is the most prominent in case A4. When the internal wave beam velocity was lower by a factor of 2.5, relative to that in cases A1–A3, incident beam degradation was not found, suggesting that there is a finite-amplitude threshold that has to be met for PSI to be operative.

[30] The selection of the subharmonic frequencies in PSI depends on the specifics of the primary wave such as the ratio of wave frequency to buoyancy frequency and Reynolds number. Case A5, with a shallower beam angle of  $7^\circ$  and larger beam velocity, is closer to oceanic conditions than cases A1–A4. The dominant subharmonic frequency in case A5 was found to be close to  $(1/2)M2$  because of the higher  $Re$ , while cases A1–A4 exhibited the pair  $0.7 M2$  and  $0.3 M2$ . The velocity in upper ocean sites with energetic internal waves is typically on the order of 0.1 m/s, which, with a buoyancy frequency of  $10^{-2} \text{ s}^{-1}$  and a beam width of 150 m, leads to  $Fr = u_0 l_b / N_1 = 0.067$  and  $Re_b = u_0 l_b / \nu = 15 \times 10^6$ . The value of  $Fr$  is similar to the values considered in the simulations, and, given the high Reynolds number, we can expect PSI with daughter waves of half the  $M2$  frequency during the interaction of such a beam with the upper ocean pycnocline. The present idealized simulations suggest that oceanic high-mode internal waves with phase-locking as in an internal wave beam are susceptible to nonlinear breakdown through subharmonic instability when they refract through the upper ocean pycnocline and, thus, may help explain the HOME observation that the energetic internal wave beams emanating from the ridge attenuate after interaction with the upper ocean pycnocline. The resonant instability generates smaller vertical scales that lead to wave steepening in the present simulations. Such wave steepening could evolve into turbulence whose properties will be examined through future three-dimensional simulations.

[31] **Acknowledgments.** We are pleased to acknowledge discussions of internal wave beam observations and the present model results with Shaun Johnston, SIO. The support of ONR N000141110512, program monitor Terri Paluszkiwicz, is gratefully acknowledged.

## References

- Akylas, T. R., R. H. Grimshaw, S. R. Clarke, and A. Tabaei (2007), Reflection tidal wave beams and local generation of solitary waves in the ocean thermocline, *J. Fluid. Mech.*, 593, 297–313.
- Alford, M. H., J. A. MacKinnon, Z. Zhao, R. Pinkel, J. Klymak, and T. Peacock (2007), Internal waves across the Pacific, *Geophys. Res. Lett.*, 34, L24601, doi: 10.1029/2007GL031566.
- Bourget, B., T. Dauxois, S. Joubaud, and P. Odier (2013), Experimental study of parametric subharmonic instability for internal plane waves, *J. Fluid. Mech.*, 723, 1–20.

- Carter, G. S., and M. C. Gregg (2006), Persistent near-diurnal internal waves observed above a site of M2 barotropic-to-baroclinic conversion, *J. Phys. Oceanogr.*, *36*, 1136–1147.
- Cole, S. T., D. L. Rudnick, B. A. Hodges, and J. P. Martin (2009), Observations of tidal internal wave beams at Kauai Channel, Hawaii, *J. Phys. Oceanogr.*, *39*, 421–436.
- Garrett, C. (2003), Internal tides and ocean mixing, *Science*, *301*, 1858–1859.
- Gayen, B., and S. Sarkar (2010), Turbulence during the generation of internal tide on a critical slope, *Phys. Rev. Lett.*, *104*, 218502–218506.
- Gayen, B., and S. Sarkar (2011a), Boundary mixing by density overturns in an internal tidal beam, *Geophys. Res. Lett.*, *38*, L14608, doi:10.1029/2011GL048135.
- Gayen, B., and S. Sarkar (2011b), Direct and large-eddy simulations of internal tide generation at a near-critical slope, *J. Fluid Mech.*, *681*, 48–79.
- Gerkema, T. (2001), Internal and interfacial tides: Beam scattering and local generation of solitary waves, *J. Mar. Res.*, *59*, 227–255.
- Gerkema, T., C. Staquet, and P. Bouruet-Aubertot (2006), Decay of semi-diurnal internal-tide beams due to subharmonic resonance, *Geophys. Res. Lett.*, *33*, L08604, doi:10.1029/2005GL025105.
- Grisouard N., C. Staquet, and T. Gerkema (2011), Generation of internal solitary waves in a pycnocline by an internal wave beam: a numerical study, *J. Fluid Mech.*, *676*, 491–513.
- Hazewinkel, J., and K. B. Winters (2011), PSI of the internal tide on a  $\beta$  plane: Flux divergence and near-inertial wave propagation, *J. Phys. Oceanogr.*, *41*, 1673–1682.
- Hibiya, T., M. Nagasawa, and Y. Niwa (2002), Nonlinear energy transfer within the oceanic internal wave spectrum at mid and high latitudes, *J. Geophys. Res.*, *107*(C11), 3207, doi:10.1029/2001JC001210.
- Holbrook, W. S., I. Fer, and R. W. Schmitt (2009), Images of internal tides near the Norwegian continental slope, *Geophys. Res. Lett.*, *36*, L00D10, doi:10.1029/2009GL038909.
- Johnston, T. M. S., D. L. Rudnick, G. S. Carter, R. E. Todd, and S. T. Cole (2010), Internal tidal beams and mixing near Monterey Bay, *J. Geophys. Res.*, *116*, C03017, doi:10.1029/2010JC006592.
- Korobov, A. S., and K. G. Lamb (2008), Interharmonics in internal gravity waves generated by tide-topography interaction, *J. Fluid. Mech.*, *611*, 61–95.
- MacKinnon, J. A., and K. B. Winters (2005), Subtropical catastrophe: Significant loss of low-mode tidal energy at 28.9°, *Geophys. Res. Lett.*, *32*, L15605, doi:10.1029/2005GL023376.
- MacKinnon, J. A., M. H. Alford, O. Sun, R. Pinkel, Z. Zhao, and J. Klymak (2013), Parametric subharmonic instability of the internal tide at 29°N, *J. Phys. Oceanogr.*, *43*, 17–28.
- Martin, J. P., D. L. Rudnick, and R. Pinkel (2006), Spatially broad observations of internal waves in the upper ocean at the Hawaiian ridge, *J. Phys. Oceanogr.*, *36*, 1085–1103.
- Mathur, M., and T. Peacock (2009), Internal wave beam propagation in non-uniform stratifications, *J. Fluid Mech.*, *639*, 133–152.
- Mercier, M. J., D. Martinand, M. Mathur, L. Gostiaux, T. Peacock, and T. Dauxois (2010), New wave generation, *J. Fluid Mech.*, *657*, 308–334.
- Mercier, M. J., M. Mathur, L. Gostiaux, T. Gerkema, J. M. Magalhaes, J. C. B. Da Silva, and T. Dauxois (2012), Soliton generation by internal tidal beams impinging on a pycnocline: Laboratory experiments, *J. Fluid Mech.*, *704*, 37–60.
- Müller, P., G. Holloway, F. Henyey, and N. Pomphrey (1986), Nonlinear interactions among internal gravity waves, *Rev. Geophys.*, *24*, 493–536.
- Nash, J. D., M. H. Alford, E. Kunze, K. Martini, and S. Kelly (2007), Hot-spots of deep ocean mixing on the Oregon continental slope, *Geophys. Res. Lett.*, *34*, L01605, doi:10.1029/2006GL028170.
- New, A. L., and R. D. Pingree (1992), Local generation of internal soliton packets in the central Bay of Biscay, *Deep Sea Res., Part A*, *39*, 1521–1534.
- Pickering, A., and M. H. Alford (2012), Velocity structure of internal tide beams emanating from Kaena Ridge, Hawaii, *J. Phys. Oceanogr.*, *42*, 1039–1044.
- Pingree, R. D., and A. L. New (1989), Downward propagation of internal tidal energy into the Bay of Biscay, *Deep Sea Res., Part A*, *36*, 735–758.
- Pingree, R. D., and A. L. New (1991), Abyssal penetration and bottom reflection of internal tidal energy in the Bay of Biscay, *J. Phys. Oceanogr.*, *21*, 28–39.
- Polzin K. L., J. M. Toole, J. R. Ledwell, and R. W. Schmitt (1997), Spatial variability of turbulent mixing in the abyssal ocean, *Science*, *276*, 93–96.
- Rainville, L., and R. Pinkel (2006), Baroclinic energy flux at the Hawaiian Ridge: Observations from the R/P FLIP, *J. Phys. Oceanogr.*, *36*, 1104–1122.
- Staquet, C., and J. Sommeria (2002), Internal gravity waves: From instabilities to turbulence, *Annu. Rev. Fluid Mech.*, *34*, 559–593.
- Sun, O., and R. Pinkel (2013), Subharmonic energy transfer from the semi-diurnal internal tide to near-diurnal motions over Kaena Ridge, Hawaii, *J. Phys. Oceanogr.*, *43*, 766–789.
- Thomas, N. H., and T. N. Stevenson (1972), A similarity solution for viscous internal waves, *J. Fluid Mech.*, *54*, 495–506.